

What are the causes of tropical cirrus longwave biases in global storm-resolving simulations?

Rachel Atlas¹, Christopher S. Bretherton¹, Adam Sokol¹, Peter Blossey¹, and Marat Khairoutdinov²

¹University of Washington

²Stony Brook University

November 24, 2022

Abstract

Cirrus control the longwave radiative budget of the tropics. For the first time, we quantify the variability in cirrus properties and longwave cloud radiative effects (CREs) that arises from using different bulk ice microphysical parameterizations within a single global storm-resolving model. We run five-day meteorologically-nudged simulations with four commonly-used microphysics schemes (M2005, Thompson, P3 and SAM1MOM) and evaluate them with satellite products and in situ observations. Tropical average longwave CRE varies over 20 W m^{-2} between schemes. Within the Thompson scheme, rapid autoconversion of cloud ice to snow leads to deficient anvil cirrus even with radiatively active snow. SAM1MOM, which uses saturation adjustment for cloud ice, also has deficient anvil cirrus. M2005 and P3 simulate cirrus with realistic frozen water path, and P3 best reproduces observed longwave CRE. Even in those schemes, ice crystal number concentrations commonly hit limiters and lack the observed variability and dependence on frozen water content.

What are the causes of tropical cirrus longwave biases in global storm-resolving simulations?

R.L. Atlas¹, C.S. Bretherton², A.B. Sokol¹, P.N. Blossey¹, M.F.
Khairoutdinov³

¹Dept. of Atmospheric Sciences, University of Washington, Seattle, WA

²Allen Institute for Artificial Intelligence, Seattle, WA

³School of Marine and Atmospheric Sciences, Stony Brook University, Stony Brook, NY

¹3920 Okanogan Ln, Seattle, WA 98195

²2157 N Northlake Way #110, Seattle, WA 98103

³Endeavour, 145, Stony Brook, NY 11790

Key Points:

- Global storm-resolving models are uniquely suited for microphysics sensitivity studies.
- Mean tropical longwave CRE biases vary over 20 W m^{-2} and cirrus coverage varies over a factor of two depending on microphysics.
- Efficiency of cloud ice sublimation and conversion to snow, and limiters on cloud ice number affect simulated cirrus.

Abstract

Cirrus control the longwave radiative budget of the tropics. For the first time, we quantify the variability in cirrus properties and longwave cloud radiative effects (CREs) that arises from using different bulk ice microphysical parameterizations within a single global storm-resolving model. We run five-day meteorologically-nudged simulations with four commonly-used microphysics schemes (M2005, Thompson, P3 and SAM1MOM) and evaluate them with satellite products and in situ observations. Tropical average longwave CRE varies over 20 W m^{-2} between schemes. Within the Thompson scheme, rapid autoconversion of cloud ice to snow leads to deficient anvil cirrus even with radiatively active snow. SAM1MOM, which uses saturation adjustment for cloud ice, also has deficient anvil cirrus. M2005 and P3 simulate cirrus with realistic frozen water path, and P3 best reproduces observed longwave CRE. Even in those schemes, ice crystal number concentrations commonly hit limiters and lack the observed variability and dependence on frozen water content.

Plain Language Summary

Recently, advancements in computing capabilities have made it possible for atmospheric scientists to simulate Earth's global atmosphere with higher resolution than ever before. This new generation of models, called global-storm resolving models, have a horizontal resolution of just a few kilometers, which is adequate to resolve thunderstorms. As a result, they simulate clouds more realistically than traditionally climate and weather models and are a great tool for diagnosing cloud biases in atmospheric models. Here, we run a single global storm-resolving model with four different representations of cloud physics called M2005, P3, SAM1MOM and Thompson. We evaluate simulated tropical cirrus clouds, which are stratiform ice clouds at the top of the troposphere that reduce the amount of infrared radiation emitted by the Earth, with satellite data to see which representations have the best performance. We find that tropical cirrus cloud coverage varies over a factor of two across the different representations, leading to differences in the amounts of infrared radiation emitted by the Earth. SAM1MOM and Thompson make too few cirrus clouds causing too much infrared radiation to be emitted, M2005 makes slightly too many cirrus causing too little infrared radiation to be emitted, and P3 makes about the right amount.

1 Introduction

Anvil cirrus, which flow outward from deep convective cores (Deng et al., 2016), reflect solar radiation and absorb longwave radiation from Earth’s surface and re-emit it at colder temperatures, thereby reducing outgoing longwave radiation and heating the atmosphere (Hartmann et al., 2001). Atmospheric models must adequately represent the formation, evolution and optical properties of anvil cirrus to reproduce the observed radiative budget of the tropics.

Anvil cirrus are sensitive to the representation of deep convection and ice microphysics. These influences are difficult to disentangle in coarse resolution global models, where both are parameterized. Global storm-resolving models, which typically have sub-5 km horizontal grid spacing and explicit rather than parameterized deep convection, provide a unique opportunity to study how ice microphysics alone influences the representation of anvil cirrus.

Nugent et al. (2022) and Turbeville et al. (2022) studied the representation of tropical deep convection, cirrus and top-of-atmosphere radiation across the set of global storm-resolving models participating in the Dynamics of the Atmospheric general circulation Modeled On Non-hydrostatic Domains (DYAMOND) project. Here, we take a complementary approach, isolating the sensitivity of anvil cirrus to ice microphysics by running one such model with four different microphysics schemes. Sullivan and Voigt (2021) used regional storm-resolving simulations to show that the representation of ice microphysics exerted strong control over the radiative budget of the Asian monsoon region. We extend their findings to the entire tropics and identify additional microphysical constraints on anvil cirrus properties.

2 Data

Four five-day global storm-resolving simulations are run with the Global System for Atmospheric Modelling (Khairoutdinov et al., 2022). They are set up identically, as described in Atlas et al. (2022), except that they are run with different bulk microphysics schemes: M2005 (Morrison et al., 2005), Thompson (Thompson et al., 2008), P3 (Morrison & Milbrandt, 2015) with one ice class, and SAM1MOM (Khairoutdinov & Randall, 2003). The differences between the schemes in their parameterizations of ice processes are summarized in Text S1. The simulations have approximately 4 km horizontal resolution in

80 the tropics and about 500 m vertical resolution between 5 and 19 km. They are initial-
 81 ized from ERA5 reanalysis (Hersbach et al., 2020) at 00 UTC 16 Feb. 2018. We analyze
 82 days 2-5 of the simulations (17-20 February 2018) throughout this study, allowing one
 83 day for model spinup, long enough for cloud statistics to equilibrate (?). Simulated
 84 temperature and horizontal winds (but not humidity or clouds) are nudged to ERA5 re-
 85 analysis with a damping timescale of 24 hours. This nudging strategy ensures that the
 86 model output can faithfully be compared with coincident real-world observations and
 87 that differences between simulated clouds can primarily be attributed to the bulk mi-
 88 crophysics schemes.

89 Simulated longwave and shortwave cloud radiative effects (CREs) are compared
 90 with coincident retrievals from Clouds and the Earth’s Radiant Energy System level 3
 91 data (Doelling et al., 2013; NASA/LARC/SD/ASDC, 2017), referred to hereafter as CERES.
 92 CERES has hourly temporal resolution and $1^\circ \times 1^\circ$ horizontal resolution.

93 Retrieved frozen water content (FWC) and effective radii (r_e) from the DARDAR-
 94 CLOUD dataset (Delanoë & Hogan, 2010) versions V2.1.0 and V3.10 (Cazenave et al.,
 95 2019) and the Cloudsat and CALIPSO Ice Cloud Property Product (2C-ICE) (Deng et
 96 al., 2015) version RF05 are used to evaluate simulated anvil cirrus microphysics and macro-
 97 physics. These retrievals have a horizontal resolution of 1.4 km, comparable to that of
 98 the simulations. The vertical resolution of DARDAR and 2C-ICE are 60 m and 240 m,
 99 respectively. We use data from the Februaries of 2007-2012.

100 Simulated microphysics are evaluated with in situ airborne observations of ice crys-
 101 tal number concentration and FWC (Krämer, Rolf, Spelten, Afchine, et al., 2020; Krämer,
 102 Rolf, & Spelten, 2020). We hereafter refer to this dataset as the ‘Microphysics Guide’.
 103 Text S2-S3 and Figures S1-S3 further discuss our use of DARDAR, 2C-ICE and the Mi-
 104 crophysics Guide.

105 **3 Microphysics schemes exhibit wide-ranging tropical longwave cloud** 106 **radiative effects**

107 Figure 1 compares simulated CREs with CERES. Throughout this study, radia-
 108 tive fluxes are defined as positive downwards, so that negative CREs indicate energy lost
 109 from the Earth. Shortwave CRE biases (panel b) are largest and most scheme-dependent
 110 over the Southern Ocean, as discussed in Atlas et al. (2022); these are sensitive to all clouds,

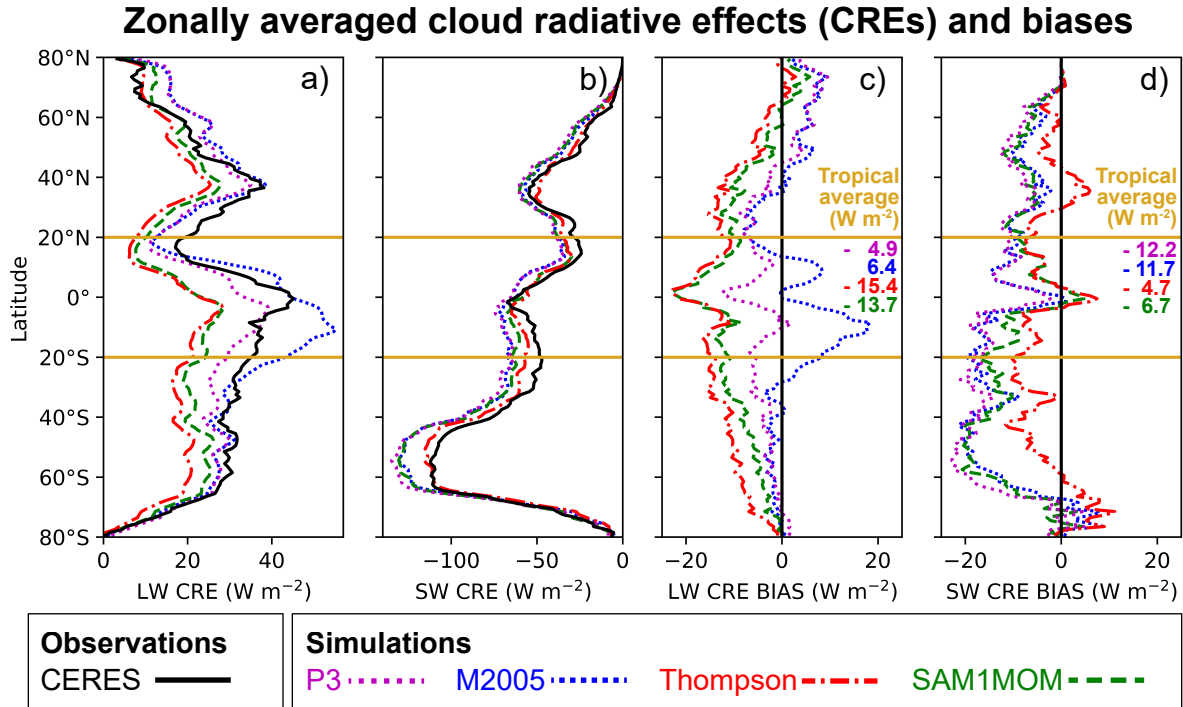


Figure 1. (a-b) Zonal average top of atmosphere CREs and (c-d) their biases vs. CERES.

Yellow lines delineate the tropical analysis region (20°S - 20°N).

111 but especially to marine boundary layer clouds because of their extensive coverage and
 112 substantial albedo. In this study, however, we focus on the region between the yellow
 113 parallel lines at 20°N and 20°S, hereafter referred to as ‘the tropics’. This is a region of
 114 strong sensitivity of longwave CRE, produced mainly by cirrus clouds, to the microphysics
 115 scheme (panel a).

116 Longwave and shortwave CRE biases for the four schemes are plotted on panels
 117 c-d. Their area-weighted tropical means (printed on the plots) vary over ranges of 7.5
 118 and 22 W m⁻², respectively. While all simulations are too bright in the shortwave, the
 119 sign of the longwave CRE bias differs between M2005, whose clouds have excessive long-
 120 wave CRE, and the other schemes. M2005 and P3 have smaller average longwave CRE
 121 biases than SAM1MOM and Thompson.

2018 Feb 20 Hour 00

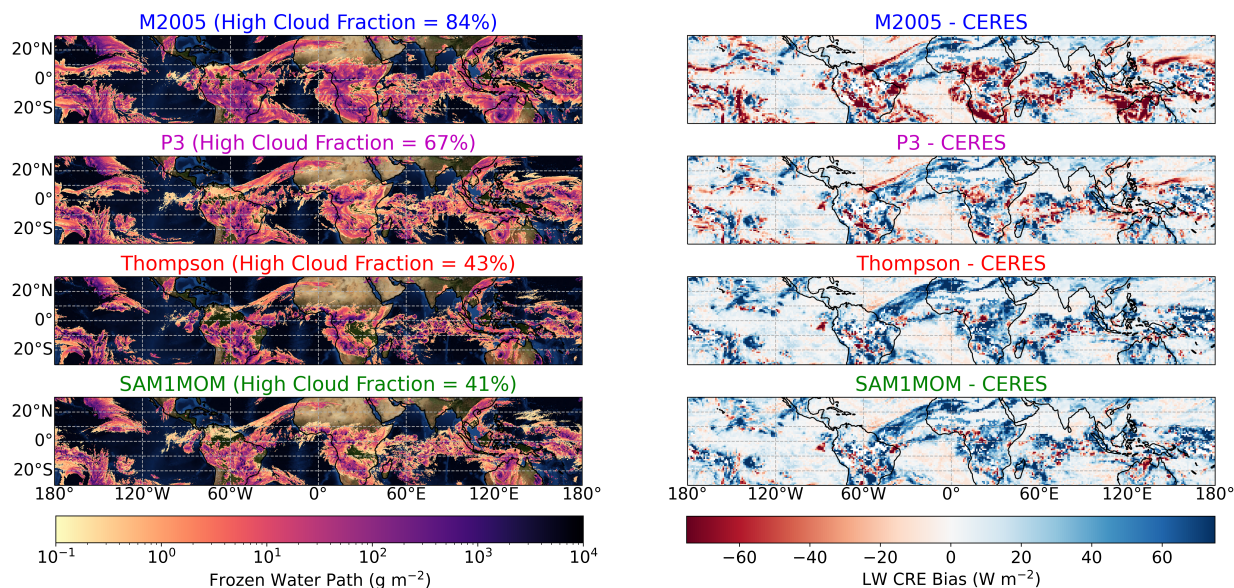


Figure 2. **left:** Snapshots of simulated FWP for columns with CTH > 10 km on the simulations' native grid. **right:** Coincident snapshots of longwave CRE bias compared to CERES on a coarsened $1^\circ \times 1^\circ$ grid.

4 Variability in anvil cirrus coverage and optical properties lead to diverse longwave cloud radiative effects

Figure 2 shows coincident snapshots at an arbitrarily-chosen time of simulated frozen water path (FWP, the sum of the cloud ice, snow and graupel water paths) for columns containing high cloud, on the left, and biases in simulated longwave CRE coarsened to a $1^\circ \times 1^\circ$ grid, on the right. Cloud top height (CTH) is defined as the highest model level with FWC (the sum of the cloud ice, snow and graupel water contents) $> 10^{-4} \text{ g m}^{-3}$ (the limit of lidar detectability as discussed in Text S2). Columns are identified as containing high cloud if they have CTH ≥ 10 km. The fraction of columns within the mapped area that meet these criteria is listed in the title of each snapshot. The coarsened longwave CRE bias is sensitive to both cloud fraction and cloud radiative properties. Animation S1 loops through versions of Figure 2 for each of the 96 hours of model output within days 2-5 of the simulations, showing that each hourly snapshot is representative of the entire four day period.

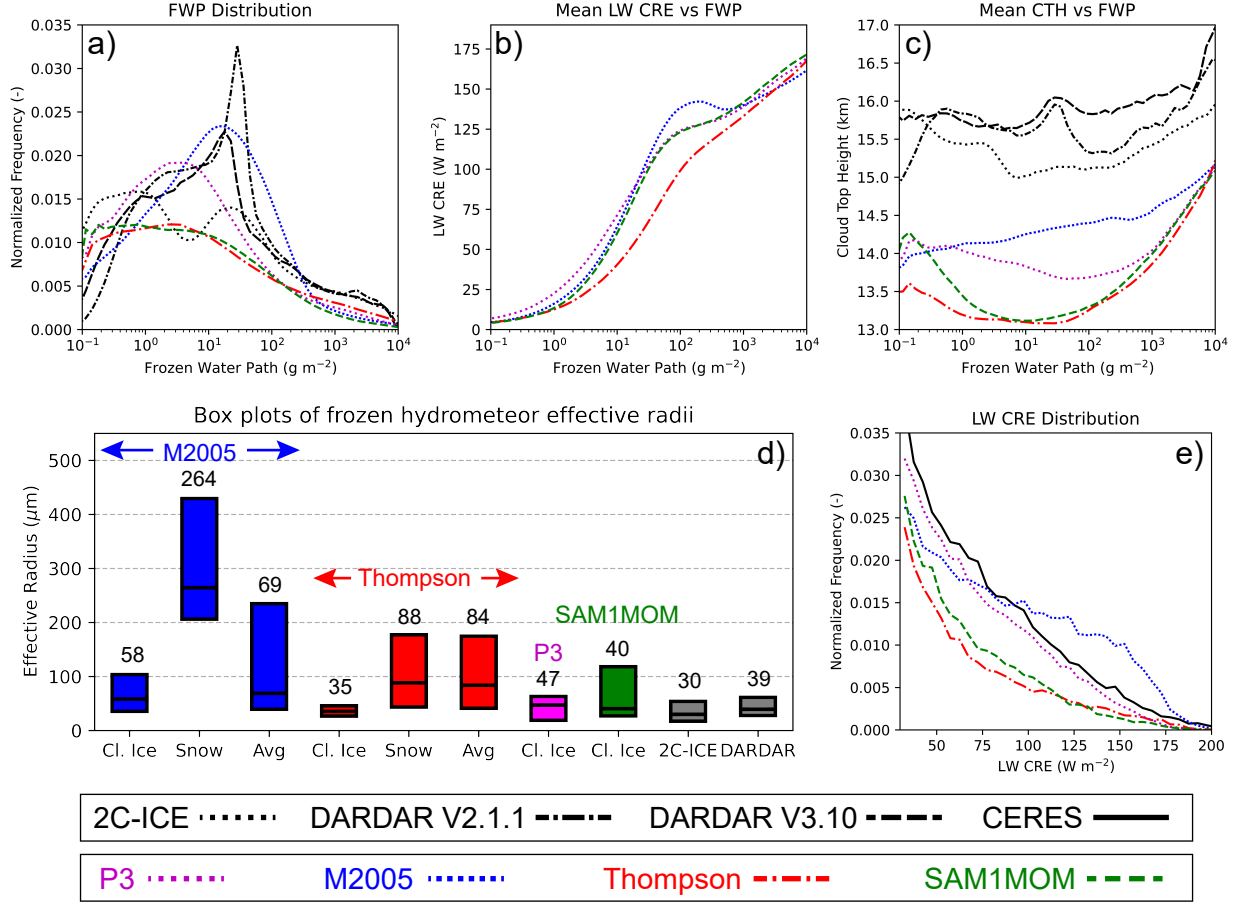


Figure 3. Tropical nighttime: **a)** PDF of FWP **b)** Mean longwave CRE, and **c)** Mean CTH, both as binned by FWP. **d)** Box plots with medians (black lines and numbers printed above each box) of frozen hydrometeor r_e . **e)** PDF of longwave CRE for $1^\circ \times 1^\circ$ boxes. Only columns with CTH > 10 km and grid cells with FWP $> 10^{-4}$ g m⁻³ are used in panels **a-d**.

136 M2005 has the largest high cloud fraction and extensive areas of negative longwave
 137 cloud biases, associated with deep convection (FWP $> 10^3$ g m⁻²) and anvil cirrus (10
 138 \leq FWP $\leq 10^3$ g m⁻²). Thompson and SAM1MOM have half of M2005's cloud frac-
 139 tion and positive longwave biases in most areas of anvil cirrus. P3's high cloud fraction
 140 lies between that of M2005 and Thompson/SAM1MOM. With a mixture of positive and
 141 negative biases associated with anvil cirrus, P3 has the fewest areas with large biases of
 142 either sign.

143 Figure 3 statistically summarizes relationships between high cloud properties and
 144 longwave cloud biases, using CERES, DARDAR and 2C-ICE to provide observational

145 constraints on the simulations. The CALIPSO lidar used by DARDAR and 2C-ICE has
 146 greater sensitivity at night, during which it can detect FWCs $\geq 10^{-4}$ g m $^{-3}$ (Text S2).
 147 Thus, we use DARDAR and 2C-ICE data from the nighttime A-train overpass, which
 148 crosses the equator at approximately 1:30 AM local time. For consistency, we also sam-
 149 ple CERES and the simulations at night. FWCs $< 10^{-4}$ g m $^{-3}$ are filtered out of the
 150 simulations and satellite retrievals.

151 In Figure 3a, we evaluate distributions of simulated FWP from columns contain-
 152 ing high cloud (CTH > 10 km) using DARDAR and 2C-ICE. The simulations and the
 153 two DARDAR datasets have unimodal distributions of FWP whereas 2C-ICE has a bi-
 154 modal distribution. The discrepancy between DARDAR and 2C-ICE for FWPs < 30 g
 155 m $^{-3}$, noted by Hong et al. (2016), emphasizes limitations on constraining FWP from CALIPSO
 156 in tropical cirrus too thin to be detected by CloudSat. For FWPs between 30 g m $^{-2}$ and
 157 300 g m $^{-2}$, M2005 and P3 bracket the observations, with P3 slightly underestimating
 158 anvil cirrus coverage, and M2005 slightly overestimating it. SAM1MOM and Thomp-
 159 son starkly underestimate anvil cirrus coverage. Satellite retrievals from deep convec-
 160 tive cores (FWPs $> 10^3$ g m $^{-2}$) are uncertain (Delanoë & Hogan, 2010) so the appar-
 161 ent low FWP bias of the simulations may not be concerning.

162 Figure 3b shows mean longwave CRE as a function of FWP for the simulations,
 163 at the model 4 km grid resolution. M2005 has the strongest longwave CRE for FWPs
 164 between 10 and 10 3 g m $^{-2}$, and Thompson has the weakest.

165 Variability in longwave CRE for a fixed FWP can be caused by differences in cloud
 166 top temperature. In the tropics, cloud top temperature is tightly linked to CTH. Fig-
 167 ure 3c shows mean CTH as a function of FWP for the simulations and the satellite re-
 168 trievals. CTH is biased low in all simulations as explained later in this section. M2005
 169 has the highest CTH for FWPs > 1 g m $^{-2}$, which contributes to its stronger longwave
 170 CRE in Figure 3b. However, CTH does not explain the differences in Figure 3b between
 171 SAM1MOM, Thompson and P3.

172 Differences between the simulated longwave CRE in Figure 3b could also come from
 173 differences in effective radii (r_e). Figure 3d shows box plots of r_e of frozen hydromete-
 174 ors for the simulations, 2C-ICE and DARDAR V3.10 (the two versions of DARDAR have
 175 similar r_e). For M2005 and Thompson, $r_{e,avg}$ is an optical depth preserving average of
 176 the cloud ice and snow effective radii, $r_{e,i}$ and $r_{e,s}$, which is directly comparable to satellite-

177 retrieved r_e . For P3, there is only one frozen hydrometeor class and for SAM1MOM, only
 178 cloud ice is radiatively active, so the snow contribution to r_e is neglected.

179 In M2005, the median $r_{e,avg}$ is similar to the median $r_{e,i}$ because cloud ice dom-
 180 inates the frozen hydrometeor mass (Figure 3d). In Thompson, the median $r_{e,avg}$ is sim-
 181 ilar to the median $r_{e,s}$ because snow dominates the frozen hydrometeor mass. This causes
 182 Thompson to have an unrealistically large $r_{e,avg}$, which contributes to it having the weak-
 183 est longwave CRE in Figure 3b. All simulations have larger average median r_e than ob-
 184 served, consistent with Stanford et al. (2017).

185 Figure 3e shows the tail of the histogram of $1^\circ \times 1^\circ$ nighttime longwave CRE for
 186 the four simulations and for CERES, which includes areas that contribute most to the
 187 tropical average and to differences between simulations and CERES. M2005 has too many
 188 areas with average longwave CRE $> 100 \text{ W m}^{-2}$ because it has more anvil cirrus than
 189 DARDAR and 2C-ICE (Figure 3a). Thompson and SAM1MOM have too few areas with
 190 average longwave CRE $> 30 \text{ W m}^{-2}$, due to deficient anvil cirrus and (for Thompson)
 191 unrealistically large r_e .

192 Figure 4 compares simulated vertical profiles of thermodynamic and cloud prop-
 193 erties with two ERA5 datasets, DARDAR and 2C-ICE. Figure 4a shows temperature
 194 profiles from ERA5 on 37 pressure levels and 137 model levels. In all simulations, tem-
 195 perature was nudged to pressure-level data (black dots), linearly interpolated to the gSAM
 196 model levels. The ERA5 model level data (black line) better resolves the 16-18 km layer,
 197 which includes the cold point at 17.3 km. All simulations have a warm bias in that layer
 198 and a cold point near 16 km instead of 17.3 km.

199 Figure 4b show profiles of average relative humidity with respect to ice (RH_i). SAM1MOM
 200 has a lower average RH_i than the other simulations and ERA5, particularly above 14
 201 km, possibly because it uses saturation adjustment for cloud ice, preventing RH_i from
 202 ever exceeding 100%. The other simulations have higher RH_i than ERA5 near the cold
 203 point, but ERA5 may be biased by its internal ice microphysical modeling assumptions
 204 in the tropical tropopause layer, where routine observations of the very low water va-
 205 por concentration are uncertain.

206 Figure 4c shows profiles of cloud fraction. For all simulations, the altitudes of max-
 207 imum cloud fraction are 2 km lower than observed, likely due to their artificially low-

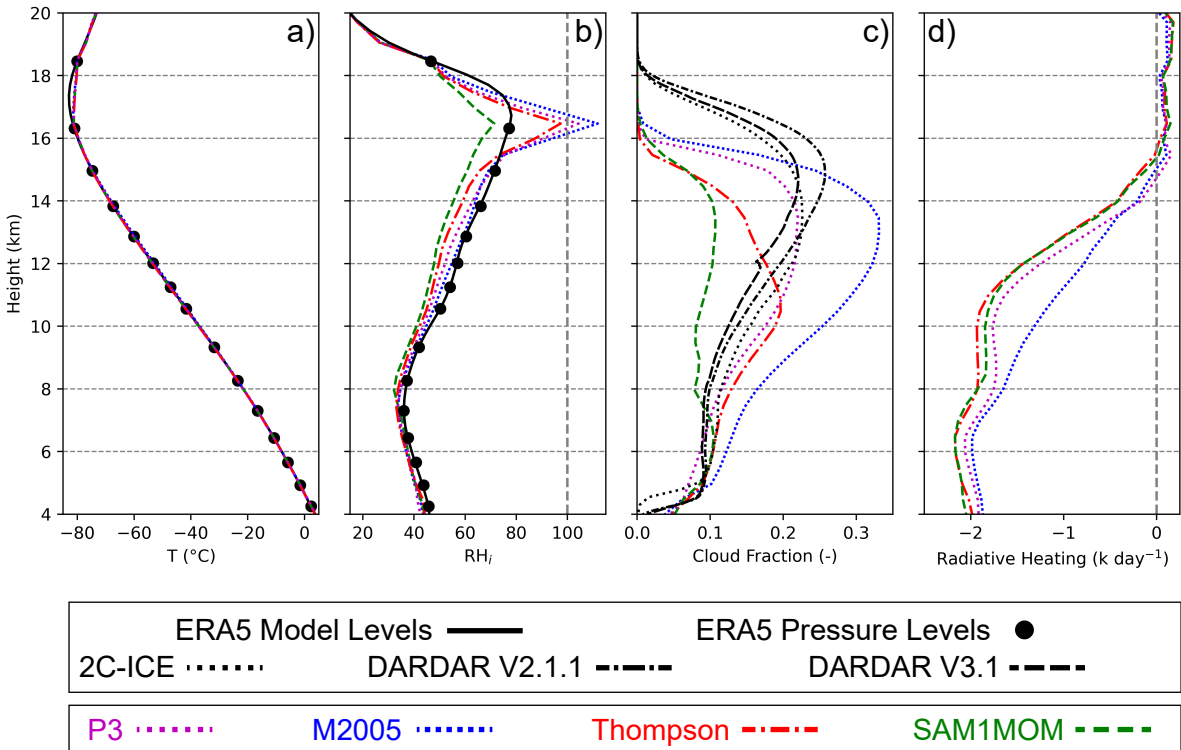


Figure 4. Vertical profiles of tropical nighttime-mean a) temperature, b) RH_i , c) cloud fraction ($FWC > 10^{-4} \text{ g m}^{-3}$ only), and d) longwave radiative cooling.

208 ered cold point altitude. Below 14.5 km, P3 agrees well with both DARDAR datasets
 209 and 2C-ICE, M2005 overestimates cloud fraction, and SAM1MOM and Thompson un-
 210 derestimate it. In M2005 and P3, cloud fraction increases monotonically up to the base
 211 of the tropical tropopause layer at 14 km. Thompson’s peak cloud fraction is only at 10.5
 212 km, likely due to excessively efficient conversion of cloud ice to quickly falling snow. SAM1MOM
 213 has a nearly constant cloud fraction throughout the troposphere.

214 Figure 4d shows longwave radiative cooling profiles for the simulations. Cirrus clouds
 215 reduce radiative cooling by absorbing upwelling longwave radiation. M2005 has up to
 216 0.5 K day^{-1} less radiative cooling than the other simulations between 8 and 13 km due
 217 to its comparably large cirrus coverage. Thompson and SAM1MOM, which have the small-
 218 est cirrus coverage, correspondingly have the strongest longwave cooling. These results
 219 are consistent with the findings of Hu et al. (2021).

220 Longwave CRE biases in the simulations can largely be explained by biases in the
 221 amount, the vertical structure, and the r_e of anvil cirrus, all of which can be estimated
 222 from spaceborne lidar and radar. These biases depend on the microphysics scheme; over-
 223 all P3 best matches remote-sensing observations, followed by M2005, with Thompson
 224 and SAM1MOM producing far too little tropical cirrus.

225 **5 Simulated ice crystal populations lack observed variability**

226 As a complementary test of the microphysics schemes, we compare simulated ice
 227 crystal number concentration (N_{ice}) and FWC with in situ airborne observations from
 228 several tropical field studies, synthesized in the Microphysics Guide (see Text S3 and Fig-
 229 ure S3), which have been coarsened to 0.04 Hz to match the horizontal resolution of the
 230 simulations. All observational data is from heights above 10 km, and latitudes between
 231 20°S and 20°N ; model histograms are accumulated from all post-spin-up output times
 232 (day and night) at all tropical high-cloud grid points.

233 Figure 5 shows 2D histograms of FWC and N_{ice} for M2005, P3, Thompson and in
 234 situ observations. SAM1MOM is omitted because it does not predict N_{ice} for any hy-
 235 drometeor classes. N_{ice} and FWC for M2005 and Thompson include cloud ice, graupel
 236 and snow. Vertical lines overlaid on the 2D histograms show limiters specified within the
 237 microphysics schemes. These limiters are designed to prevent algorithms within the schemes
 238 from producing physically implausible results; if the limiter is frequently active, this sug-

239 gests problems with parameterization assumptions made within the scheme. Dotted lines
 240 show limiters on total cloud ice concentration and dashed lines show limiters on the con-
 241 centration of ice particles produced through deposition nucleation, which is the domi-
 242 nant mode of nucleation within the temperature range investigated here. In Thompson,
 243 the two limiters are the same.

244 In M2005 and P3, most grid cells have values of N_{ice} that are very close to the smaller
 245 of these two limiters, which are 0.3 and 0.1 cm^{-3} , respectively. They have higher mean
 246 N_{ice} than the in situ observations and lack the observed variability in N_{ice} and depen-
 247 dence of N_{ice} on FWC. In the 2D histogram for P3, the grid cells between the two lim-
 248 iter values, which primarily have high FWCs, have experienced homogeneous freezing
 249 of cloud droplets. There is no homogeneous freezing of aerosol in any microphysics schemes
 250 used here. Thompson has many grid cells with tiny FWC and N_{ice} and a subpopulation
 251 of grid cells dominated by snow (a large ratio of FWC to N_{ice}) as a result of efficiently
 252 converting most cloud ice to snow. Although P3 lacks the observed variability, its mean
 253 N_{ice} is closest to the observed mean.

254 **6 Conclusions**

255 Tropical longwave cloud radiative effects (CREs) simulated by a global storm-resolving
 256 model are sensitive to ice microphysics. Average biases in longwave CRE vary over a 22
 257 W m^{-2} range across four simulations which differ only in their microphysical schemes,
 258 due to variability in cirrus amount, thickness, cloud top height, and ice crystal number
 259 and size.

260 Simulations run with Thompson and SAM1MOM microphysics had very weak long-
 261 wave CREs. The Thompson scheme quickly converts cloud ice to larger snow particles,
 262 which fall quickly and reduce cirrus cloud cover, and decrease the optical depth of the
 263 remaining cirrus, even though the snow is radiatively active. SAM1MOM's small cirrus
 264 coverage may be related to the instantaneous sublimation of sedimenting cloud ice in sub-
 265 saturated conditions.

266 The other two simulations, run with M2005 and P3 microphysics, had stronger long-
 267 wave CREs which agreed better with satellite observations. M2005's cirrus coverage is
 268 larger than observed, causing it to overestimate longwave CRE. P3's cirrus coverage is
 269 slightly smaller than observed, causing a slight underestimation of longwave CRE. Sim-

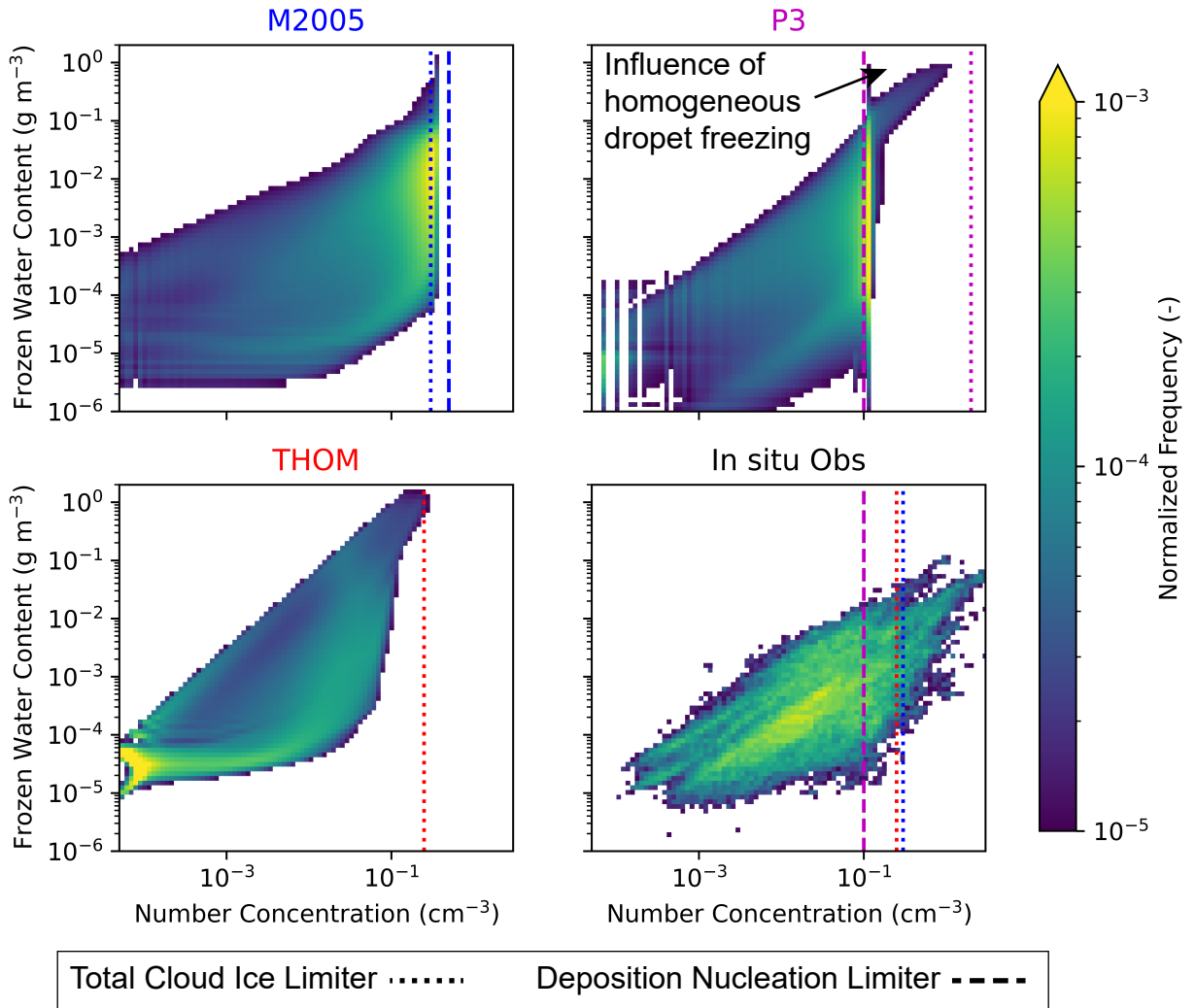


Figure 5. 2D histograms of FWC (on the y-axis) and N_{ice} (on the x-axis). Dashed and dotted lines indicate limiters on total cloud ice number concentration and cloud ice particles that can be formed through deposition nucleation, respectively.

270 ulated ice crystal number concentrations in M2005 and P3 ubiquitously hit arbitrary lim-
271 iters within the microphysics schemes. As a result, typical ice crystal number concen-
272 trations lack the observed variability and dependence on frozen water content. P3 lim-
273 its ice concentrations to be a factor of three lower than M2005; this discrepancy may ac-
274 count for most of their differences in anvil cirrus coverage and thickness. Overall, P3 per-
275 formed most skillfully of the four tested schemes across our diverse suite of observational
276 comparisons.

277 Our results may have some sensitivity to model setup and forcing. The gSAM DYAMOND
278 simulation, run with SAM1MOM, agreed considerably better with observations
279 in regional analyses of the tropics (Nugent et al., 2022; Turbeville et al., 2022) than the
280 SAM1MOM simulation evaluated here. DYAMOND was free-running rather than nudged,
281 in boreal summer rather than austral summer, and used a slightly different tuning of SAM1MOM.
282 While the relative differences between microphysical parameterizations are likely insen-
283 sitive to these configuration differences, they could have a larger effect on the observa-
284 tional comparisons. We recommend further study of this important issue.

285 Adequately representing tropical convectively initiated cirrus is necessary for con-
286 straining tropical longwave CREs in global atmospheric models. Global storm-resolving
287 models, which resolve deep convection, provide a unique opportunity to examine the sen-
288 sitivities of anvil cirrus to the choice of ice microphysics scheme and identify important
289 control parameters within schemes. We find that overly efficient autoconversion of cloud
290 ice to snow causes deficient anvil cirrus. Tropical cirrus ice crystal formation and loss
291 mechanisms need to be more realistically represented (a challenge), so that ice crystal
292 number concentrations are not overly controlled by arbitrary limiters. While we focus
293 on tropical cirrus here, global storm-resolving models have great potential for evaluat-
294 ing and improving the microphysical representation of clouds and precipitation across
295 all climate regimes.

296 **7 Open Research**

297 CERES(NASA/LARC/SD/ASDC, 2017), 2C-ICE R05 ([https://www.cloudsat](https://www.cloudsat.cira.colostate.edu/data-products/2c-ice)
298 [.cira.colostate.edu/data-products/2c-ice](https://www.cloudsat.cira.colostate.edu/data-products/2c-ice)), DARDAR-CLOUD V2.1.0 and V3.10
299 (<http://www.icare.univ-lille1.fr>), and the Microphysics Guide (Krämer, Rolf, &
300 Spelten, 2020) are publicly available online. Simulated model output cannot be made

301 available due to the experimental nature of the simulations and the large storage space
302 required.

303 **Acknowledgments**

304 We acknowledge funding from U.S. National Science Foundation (NSF) grant OISE-1743753,
305 high-performance computing support from Cheyenne (doi:10.5065/D6RX99HX) provided
306 by NCAR's Computational and Information Systems Laboratory, sponsored by NSF, and
307 Blaž Gasparini and Maximilien Bolot for helpful discussions.

308 **References**

- 309 Atlas, R., Bretherton, C. S., Khairoutdinov, M. F., & Blossey, P. N. (2022). Hallett-
310 mossop rime splintering dims cumulus clouds over the southern ocean: New
311 insight from nudged global storm-resolving simulations. *AGU Advances*, *3*(2),
312 e2021AV000454. doi: <https://doi.org/10.1029/2021AV000454>
- 313 Cazenave, Q., Ceccaldi, M., Delanoë, J., Pelon, J., Groß, S., & Heymsfield, A.
314 (2019). Evolution of dardar-cloud ice cloud retrievals: new parameters and
315 impacts on the retrieved microphysical properties. *Atmos. Meas. Tech.*, *12*(5),
316 2819-2835. (AMT) doi: 10.5194/amt-12-2819-2019
- 317 Cooper, W. A. (1986). Ice initiation in natural clouds. *Meteorological Monographs*,
318 *21*(43), 29-32. doi: 10.1175/0065-9401-21.43.29
- 319 Delanoë, J., & Hogan, R. J. (2010). Combined cloudsat-calipso-modis retrievals
320 of the properties of ice clouds. *Journal of Geophysical Research: Atmospheres*,
321 *115*(D4). doi: <https://doi.org/10.1029/2009JD012346>
- 322 Deng, M., Mace, G. G., & Wang, Z. (2016). Anvil productivities of tropical deep
323 convective clusters and their regional differences. *Journal of the Atmospheric*
324 *Sciences*, *73*(9), 3467-3487. doi: 10.1175/jas-d-15-0239.1
- 325 Deng, M., Mace, G. G., Wang, Z., & Berry, E. (2015). Cloudsat 2c-ice product
326 update with a new ze parameterization in lidar-only region. *Journal of Geo-*
327 *physical Research: Atmospheres*, *120*(23), 12,198-12,208. doi: [https://doi.org/](https://doi.org/10.1002/2015JD023600)
328 [10.1002/2015JD023600](https://doi.org/10.1002/2015JD023600)
- 329 Doelling, D. R., Loeb, N. G., Keyes, D. F., Nordeen, M. L., Morstad, D., Nguyen,
330 C., ... Sun, M. (2013). Geostationary enhanced temporal interpolation for
331 ceres flux products. *Journal of Atmospheric and Oceanic Technology*, *30*(6),

- 332 1072-1090. doi: 10.1175/jtech-d-12-00136.1
- 333 Hartmann, D. L., Moy, L. A., & Fu, Q. (2001). Tropical convection and the energy
334 balance at the top of the atmosphere. *Journal of Climate*, *14*(24), 4495-4511.
335 doi: 10.1175/1520-0442(2001)014<4495:tcateb>2.0.co;2
- 336 Hersbach, H., Bell, B., Berrisford, P., Hirahara, S., Horányi, A., Muñoz-Sabater, J.,
337 ... Thépaut, J.-N. (2020). The era5 global reanalysis. *Quarterly Journal of*
338 *the Royal Meteorological Society*, *146*(730), 1999-2049. doi: 10.1002/qj.3803
- 339 Hong, Y., Liu, G., & Li, J.-L. F. (2016). Assessing the radiative effects of global
340 ice clouds based on cloudsat and calipso measurements. *Journal of Climate*,
341 *29*(21), 7651-7674. doi: 10.1175/jcli-d-15-0799.1
- 342 Hu, Z., Lamraoui, F., & Kuang, Z. (2021). Influence of upper-troposphere stratifi-
343 cation and cloud-radiation interaction on convective overshoots in the tropical
344 tropopause layer. *Journal of the Atmospheric Sciences*, *78*(8), 2493-2509. doi:
345 10.1175/jas-d-20-0241.1
- 346 Jensen, E. J., Pfister, L., Jordan, D. E., Bui, T. V., Ueyama, R., Singh, H. B.,
347 ... Pfeilsticker, K. (2017). The nasa airborne tropical tropopause ex-
348 periment high-altitude aircraft measurements in the tropical western pa-
349 cific. *Bulletin of the American Meteorological Society*, *98*(1), 129-+. doi:
350 10.1175/bams-d-14-00263.1
- 351 Khairoutdinov, M. F., Blossey, P. N., & Bretherton, C. S. (2022). Global system for
352 atmospheric modeling: Model description and preliminary results. *Earth and*
353 *Space Science Open Archive*, *39*. doi: doi:10.1002/essoar.10509977.1
- 354 Khairoutdinov, M. F., & Randall, D. A. (2003). Cloud resolving modeling of
355 the arm summer 1997 iop: Model formulation, results, uncertainties, and
356 sensitivities. *Journal of the Atmospheric Sciences*, *60*(4), 607-625. doi:
357 10.1175/1520-0469(2003)060<0607:crmota>2.0.co;2
- 358 Krämer, M., Rolf, C., & Spelten, N. (2020). *The cirrus guide ii in-situ aircraft data*
359 *set*. doi: 10.34730/266ca2a41f4946ff97d874bfa458254c
- 360 Krämer, M., Rolf, C., Spelten, N., Afchine, A., Fahey, D., Jensen, E., ... Sourdeval,
361 O. (2020). A microphysics guide to cirrus – part 2: Climatologies of clouds and
362 humidity from observations. *Atmos. Chem. Phys.*, *20*(21), 12569-12608. (ACP)
363 doi: 10.5194/acp-20-12569-2020
- 364 Morrison, H., Curry, J. A., & Khvorostyanov, V. I. (2005). A new double-moment

- 365 microphysics parameterization for application in cloud and climate models.
366 part i: Description. *Journal of the Atmospheric Sciences*, 62(6), 1665-1677.
367 doi: 10.1175/jas3446.1
- 368 Morrison, H., & Milbrandt, J. A. (2015). Parameterization of cloud microphysics
369 based on the prediction of bulk ice particle properties. part i: Scheme descrip-
370 tion and idealized tests. *Journal of the Atmospheric Sciences*, 72(1), 287-311.
371 doi: 10.1175/jas-d-14-0065.1
- 372 NASA/LARC/SD/ASDC. (2017). *Ceres and geo-enhanced toa, within-atmosphere*
373 *and surface fluxes, clouds and aerosols 1-hourly terra edition4a*. NASA Lang-
374 ley Atmospheric Science Data Center DAAC. doi: 10.5067/TERRA+AQUA/
375 CERES/SYN1DEG-1HOUR_L3.004A
- 376 Nugent, J. M., Turbeville, S. M., Bretherton, C. S., Blossey, P. N., & Ackerman,
377 T. P. (2022). Tropical cirrus in global storm-resolving models: 1. role
378 of deep convection. *Earth and Space Science*, 9(2), e2021EA001965. doi:
379 <https://doi.org/10.1029/2021EA001965>
- 380 Pan, L. L., Atlas, E. L., Salawitch, R. J., Honomichl, S. B., Bresch, J. F., Randel,
381 W. J., ... Wolfe, G. (2017). The convective transport of active species in the
382 tropics (contrast) experiment. *Bulletin of the American Meteorological Society*,
383 98(1), 106-128. doi: 10.1175/bams-d-14-00272.1
- 384 Stanford, M. W., Varble, A., Zipser, E., Strapp, J. W., Leroy, D., Schwarzenboeck,
385 A., ... Protat, A. (2017). A ubiquitous ice size bias in simulations of trop-
386 ical deep convection. *Atmos. Chem. Phys.*, 17(15), 9599-9621. (ACP) doi:
387 10.5194/acp-17-9599-2017
- 388 Sullivan, S. C., & Voigt, A. (2021). Ice microphysical processes exert a strong con-
389 trol on the simulated radiative energy budget in the tropics. *Communications*
390 *Earth & Environment*, 2(1), 137. doi: 10.1038/s43247-021-00206-7
- 391 Thompson, G., Field, P. R., Rasmussen, R. M., & Hall, W. D. (2008). Explicit fore-
392 casts of winter precipitation using an improved bulk microphysics scheme. part
393 ii: Implementation of a new snow parameterization. *Monthly Weather Review*,
394 136(12), 5095-5115. doi: 10.1175/2008mwr2387.1
- 395 Toon, O. B., Starr, D. O., Jensen, E. J., Newman, P. A., Platnick, S., Schoe-
396 berl, M. R., ... Pickering, K. E. (2010). Planning, implementation, and
397 first results of the tropical composition, cloud and climate coupling experi-

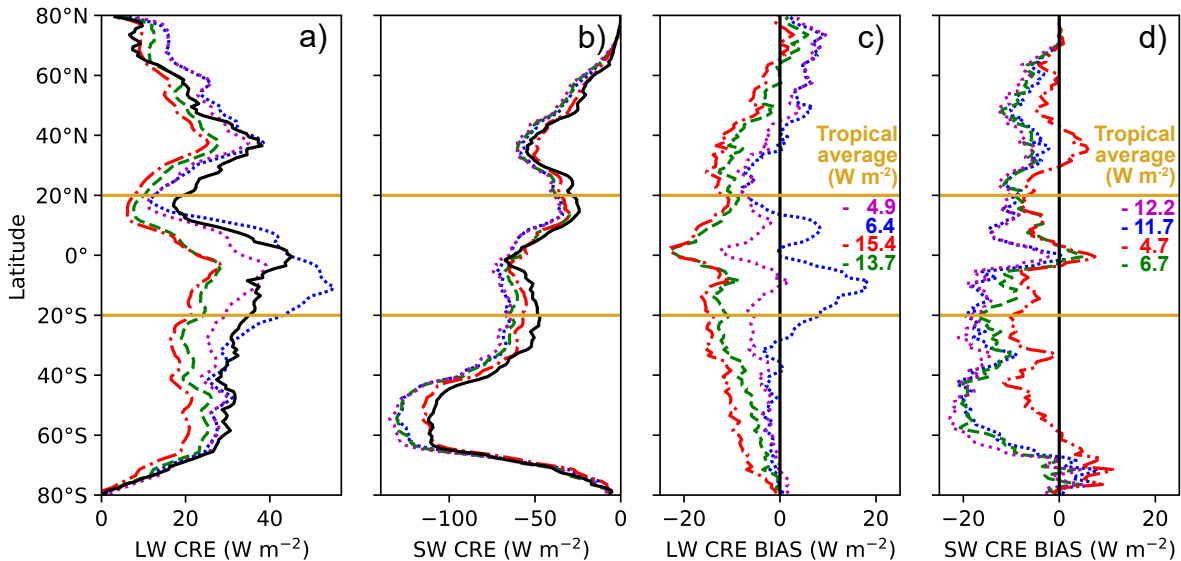
398 ment (tc4). *Journal of Geophysical Research: Atmospheres*, 115(D10). doi:
399 <https://doi.org/10.1029/2009JD013073>

400 Turbeville, S. M., Nugent, J. M., Ackerman, T. P., Bretherton, C. S., & Blossey,
401 P. N. (2022). Tropical cirrus in global storm-resolving models: 2. cirrus life
402 cycle and top-of-atmosphere radiative fluxes. *Earth and Space Science*, 9(2),
403 e2021EA001978. doi: <https://doi.org/10.1029/2021EA001978>

404 Wendisch, M., Pöschl, U., Andreae, M. O., Machado, L. A. T., Albrecht, R.,
405 Schlager, H., . . . Zöger, M. (2016). Acridicon–chuva campaign: Studying
406 tropical deep convective clouds and precipitation over amazonia using the new
407 german research aircraft halo. *Bulletin of the American Meteorological Society*,
408 97(10), 1885-1908. doi: 10.1175/bams-d-14-00255.1

Figure 1.

Zonally averaged cloud radiative effects (CREs) and biases



Observations

CERES ———

Simulations

P3 ·····

M2005 ·····

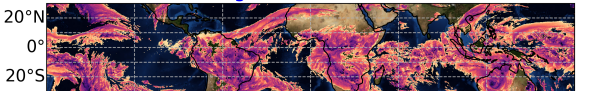
Thompson - - - -

SAM1MOM - - - -

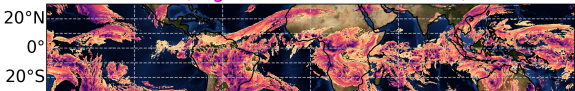
Figure 2.

2018 Feb 20 Hour 00

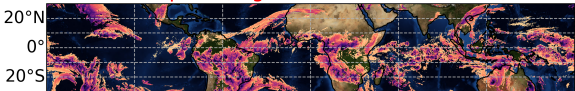
M2005 (High Cloud Fraction = 84%)



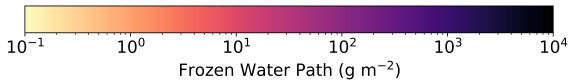
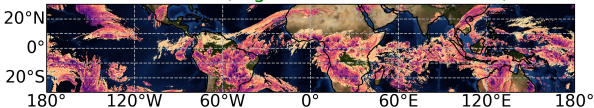
P3 (High Cloud Fraction = 67%)



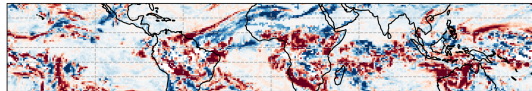
Thompson (High Cloud Fraction = 43%)



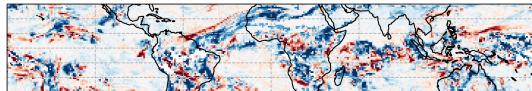
SAM1MOM (High Cloud Fraction = 41%)



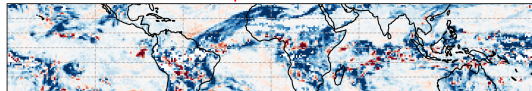
M2005 - CERES



P3 - CERES



Thompson - CERES



SAM1MOM - CERES

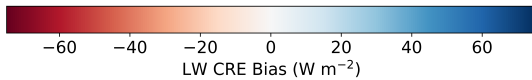
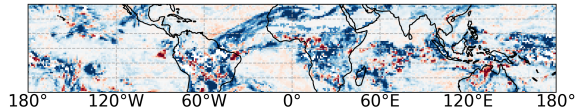
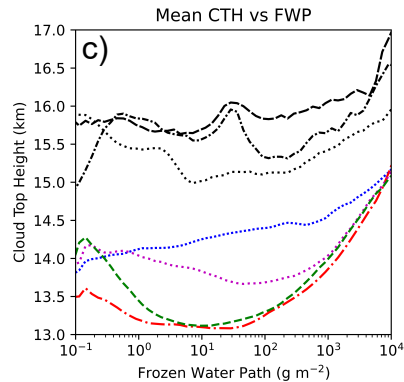
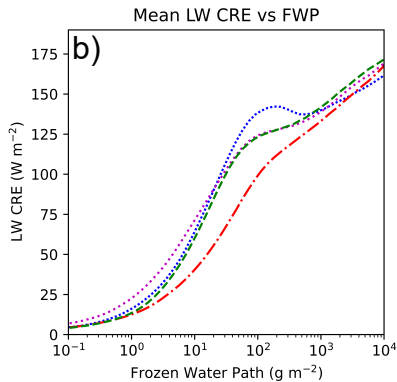
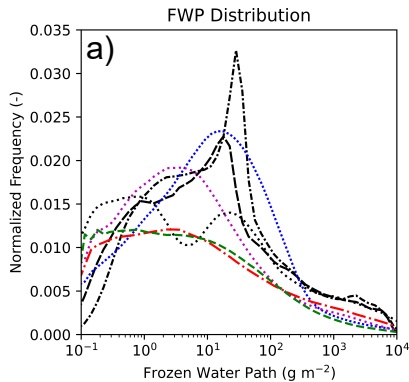
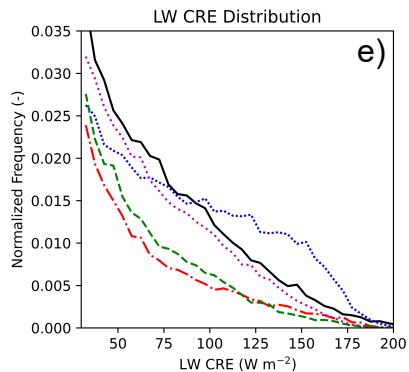
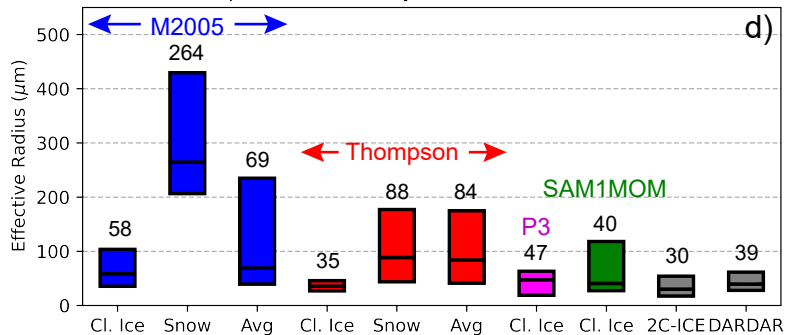


Figure 3.



Box plots of frozen hydrometeor effective radii



2C-ICE DARDAR V2.1.1 - - - - DARDAR V3.10 - · - · - CERES ———

P3 M2005 Thompson - · - · - SAM1MOM - - - -

Figure 4.

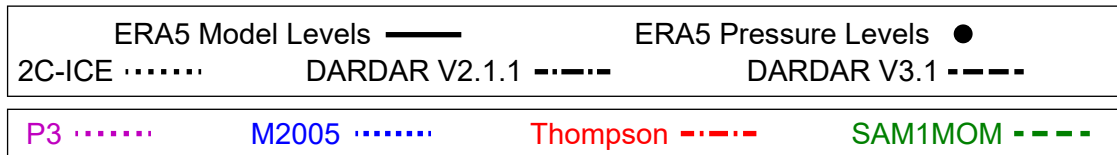
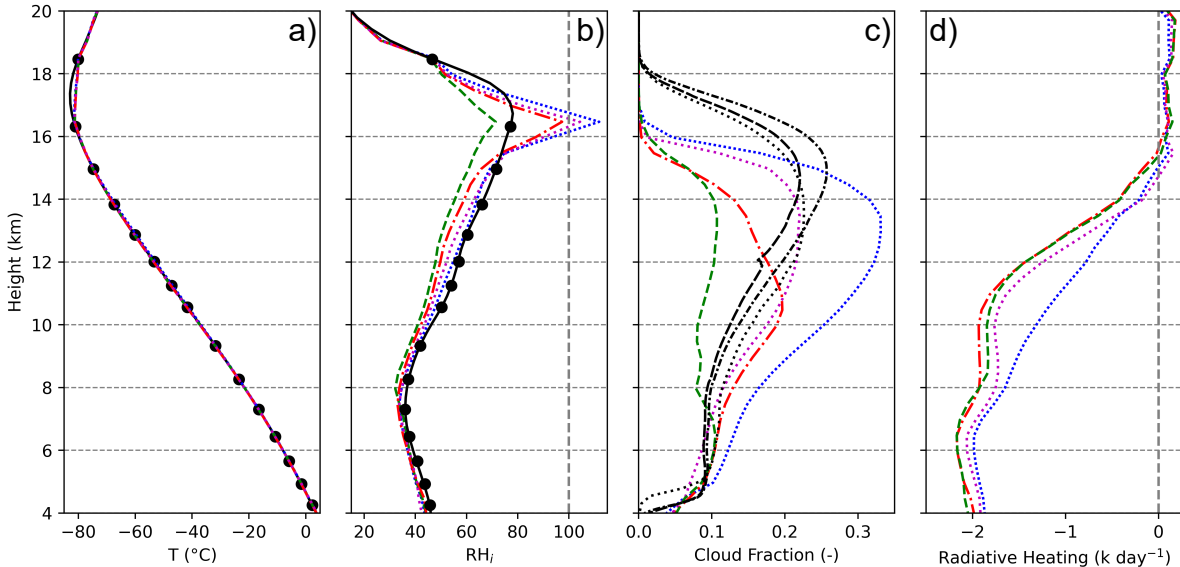
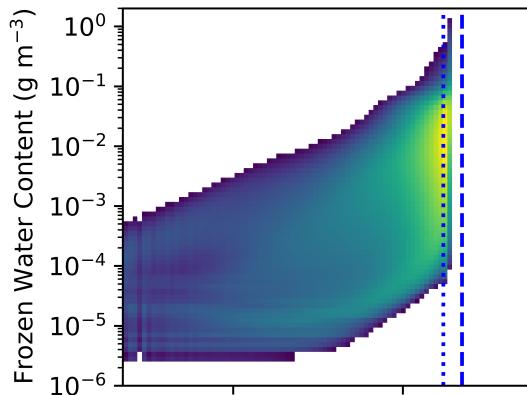
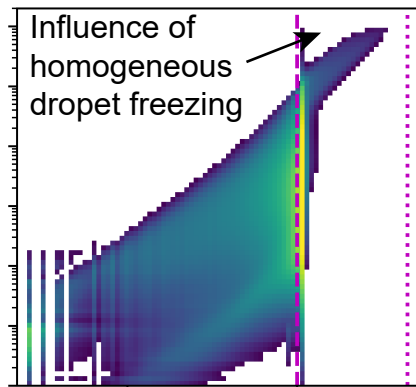


Figure 5.

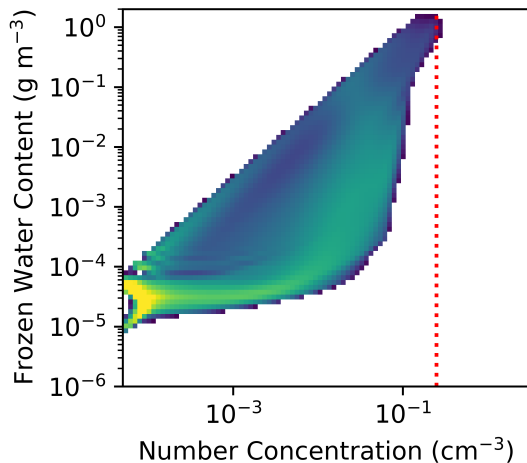
M2005



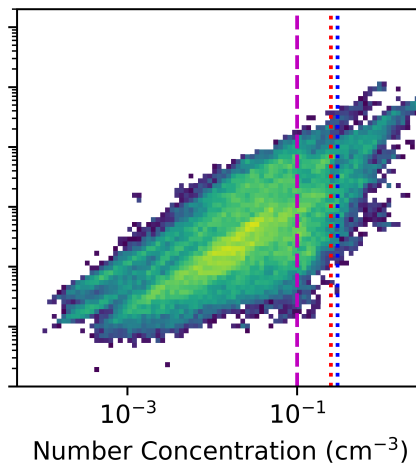
P3



THOM



In situ Obs



Normalized Frequency (-)

Total Cloud Ice Limiter

Deposition Nucleation Limiter - - -

Supporting Information for “What are the causes of tropical cirrus longwave biases in global storm-resolving simulations?”

R.L. Atlas¹, C.S. Bretherton², A.B. Sokol¹, P.N. Blossey¹, M.F.

Khairoutdinov³

¹Dept. of Atmospheric Sciences, University of Washington, Seattle, WA

²Allen Institute for Artificial Intelligence, Seattle, WA

³School of Marine and Atmospheric Sciences, Stony Brook University, Stony Brook, NY

¹3920 Okanogan Ln, Seattle, WA 98195

²2157 N Northlake Way #110, Seattle, WA 98103

³Endeavour, 145, Stony Brook, NY 11790

Contents of this file

1. Text S1 to S3
2. Figures S1 to S3

Additional Supporting Information (File uploaded separately)

1. Caption for Movie S1

Text S1: Description of ice microphysics in the four different microphysics schemes

In SAM1MOM (Khairoutdinov & Randall, 2003), two prognostic variables represent all water species: (1) total water mass mixing ratio, which combines water vapor and non-precipitating hydrometeors and (2) the precipitating hydrometeor mass mixing ratio. Both non-precipitating (cloud liquid and cloud ice) and precipitating (rain, snow and graupel) hydrometeors are partitioned between liquid and ice phases based on temperature, and ice phase precipitating hydrometeor mass is further partitioned between snow and graupel based on temperature. Only cloud ice is radiatively active. SAM1MOM partitions total water into water vapor and cloud condensate using saturation adjustment at all temperatures, including for cloud ice. This means that cloud ice condenses and sublimates instantaneously at ice saturation. M2005 (Morrison et al., 2005) predicts number and mass for three frozen hydrometeor classes (cloud ice, snow and graupel), and cloud ice and snow are both radiatively active. Thompson (Thompson et al., 2008) predicts mass for three frozen hydrometeor classes (cloud ice, snow and graupel) and number for cloud ice only. Snow number is prescribed as a function of snow mass and temperature. Cloud ice and snow are both radiatively active. P3 (Morrison & Milbrandt, 2015) is run with one radiatively active ice class, for which it predicts mass, number, rime volume and rime mass.

M2005, Thompson and P3 heterogeneously nucleate ice through deposition and immersion freezing. M2005 also includes contact nucleation. At the temperatures and heights examined here, deposition nucleation dominates heterogeneous nucleation.

In M2005, deposition nucleation occurs when either ice supersaturation exceeds 8% or the air is saturated with respect to liquid and colder than -12°C . In Thompson, it occurs when either ice supersaturation exceeds 25% or air is saturated with respect to liquid and colder than -12°C .

In P3, it occurs when the temperature is below -15°C and ice supersaturation exceeds 5%. All three schemes use the Cooper curve (Cooper, 1986) to specify the concentration of ice nucleating particles for deposition nucleation and have limiters which specify a maximum concentration of ice particles that can be formed by deposition nucleation. The limiters in P3, M2005, and Thompson are .1, .25 and .5 cm^{-3} , respectively.

All three microphysics schemes also support homogeneous freezing of droplets and raindrops when the air temperature is $< -40^{\circ}\text{C}$ but do not support homogeneous freezing of aerosol. Limiters act to restrict the total concentrations of cloud ice particles to be no larger than 2, .3 and .25 cm^{-3} in P3, M2005 and Thompson, respectively.

Text S2: Processing of DARDAR and 2C-ICE

DARDAR and 2C-ICE both retrieve frozen water content (FWC) from Cloud-Aerosol Lidar and Infrared Pathfinder Satellite Observation (CALIPSO) lidar attenuated backscatter and CloudSat radar reflectivity. A major difference between the two retrievals is that 2C-ICE parameterizes radar reflectivity for grid cells where the cloud is too thin to be detected by the CloudSat radar (Deng et al., 2015). Here, we compare retrievals of frozen water content (FWC) and frozen water path (FWP) between DARDAR V3.10 and 2C-ICE to examine the impact of that difference. Because the two versions of DARDAR are more similar to each other than they are to the 2C-ICE, we only examine the newer version of DARDAR here.

Figure S1 shows distributions of FWC from the two satellite retrievals broken up into daytime and nighttime measurements, and, in the bottom three rows, according to which instruments the retrieval is coming from (lidar only, radar only or both). In general, retrieved FWCs are smaller in 2C-ICE than in DARDAR. Most of this differences comes from lidar-only regions, where 2C-

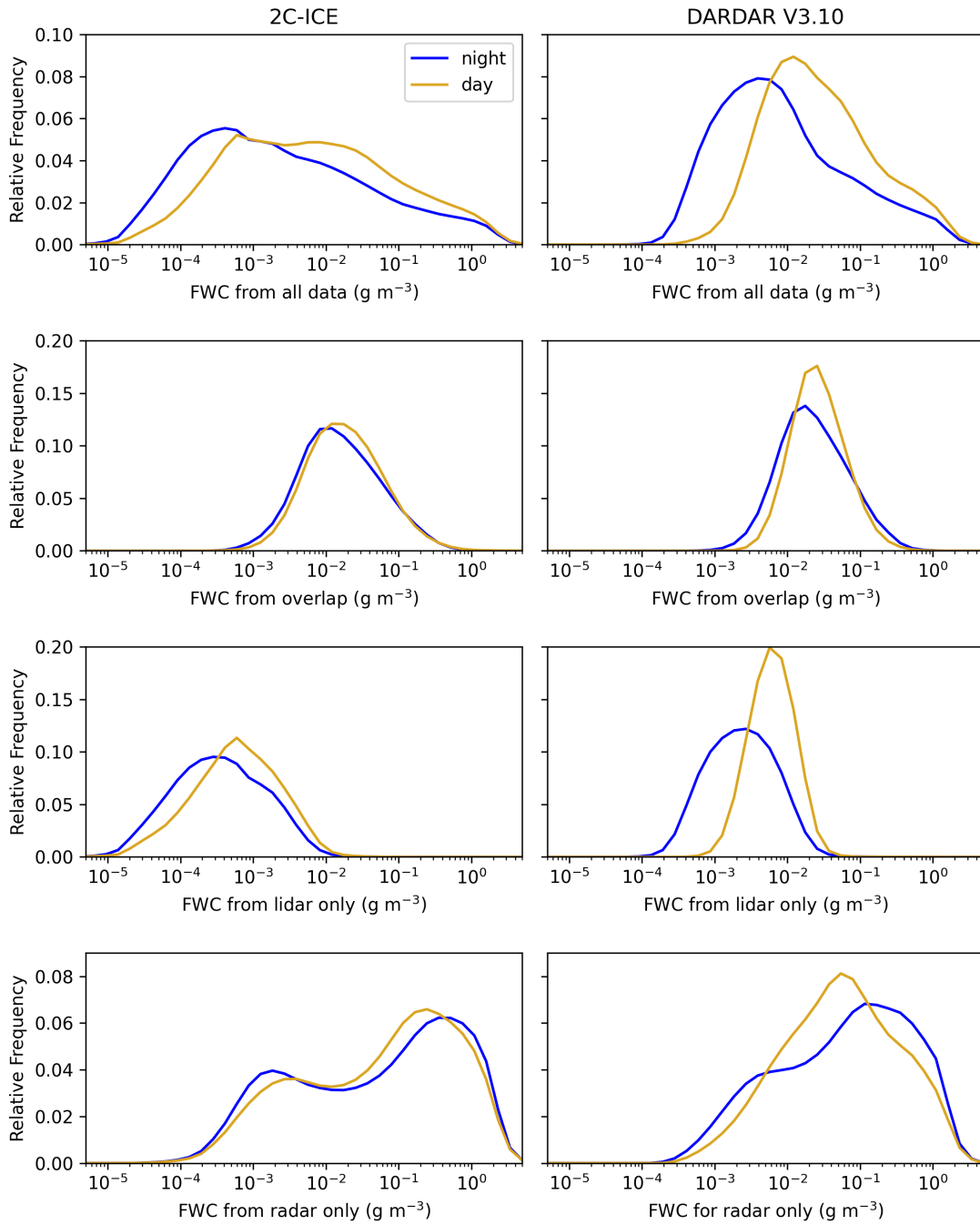


Figure S1. Distributions of FWC from nighttime and daytime measurements separately for (top to bottom row) all data, regions sensed by both the radar and lidar, lidar only regions, and radar only regions, for 2C-ICE (left) and DARDAR (right).

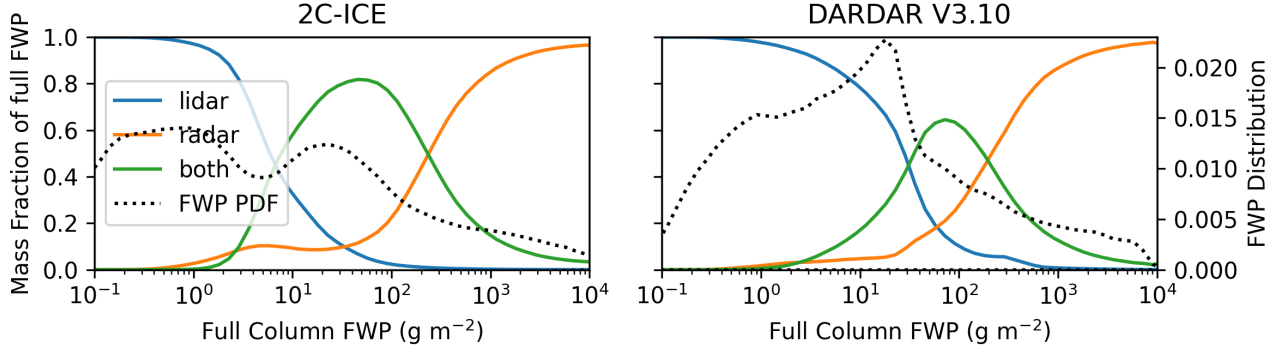


Figure S2. Blue, orange and green lines show the average mass fraction of a column that is sensed by the lidar only, radar only, and both instruments, respectively, as a function of column FWP.

ICE returns FWCs that are one order of magnitude smaller on average than those retrieved by DARDAR. 2C-ICE also has a more bimodal distribution than DARDAR for radar-only regions. The two retrievals agree best for regions with both instruments.

DARDAR's retrievals show a greater diurnal dependence, particular in the lidar-only regions, due to the fact that the lidar is more sensitive at night. Because DARDAR has greater sensitivity at night, we restrict our comparisons between the simulations and satellite retrievals to nighttime measurements. Additionally, because DARDAR cannot detect FWCs $< 10^{-4} \text{ g m}^{-3}$ at night, we filter FWCs smaller than that out of both the simulated output and the satellite retrievals before computing FWP.

Given that the retrievals diverge most from each other in lidar only regions, we examine the mass fraction that comes from lidar-only regions, radar-only regions and regions with both instruments as a function of FWP in Figure S2 (left y-axis). Distributions of FWP are overlaid (right y-axis). For FWCs $> 30 \text{ g m}^{-2}$, most of the FWP comes from regions with both instruments

or with radar only. Accordingly, the two retrievals agree well within this range. For FWPs $< 30 \text{ g m}^{-2}$, the satellite retrievals are very different from each other and do not provide as tight a constraint on the simulations.

Text S3: Processing of the Microphysics Guide

The Microphysics Guide (Krämer, Rolf, Spelten, Afchine, et al., 2020; Krämer, Rolf, & Spelten, 2020) includes quality controlled microphysics and thermodynamics observations from 24 field campaigns. Five of those campaigns measured FWC and ice crystal number concentration (N_{ice}) at latitudes between 20°S and 20°N and altitudes $> 10 \text{ km}$, including Airborne Tropical Tropopause Experiment (Jensen et al., 2017, ATTREX), Convective Transport of Active Species in the Tropics Experiment (Pan et al., 2017, CONTRAST), Aerosol, Cloud, Precipitation, and Radiation Interactions and Dynamics of Convective Cloud Systems (Wendisch et al., 2016, ACRIDICON), Tropical Composition, Cloud and Climate Coupling Experiment (Toon et al., 2010, TC4), and Pacific Oxidants, Sulfur, Ice, Dehydration, and cONvection (POSIDON). Figure S3 shows the flight tracks from all five campaigns, and lists the instruments used to measure or compute FWC and N_{ice} .

All data in the Microphysics Guide has a resolution of 1 Hz. Air speeds in the upper troposphere are typically 200 m s^{-1} , so we coarsened the data to .04 Hz (or 25 seconds) so that each data point would correspond to an approximately 5 km horizontal distance, and better match the spacial scale of the simulated output. The numbers next to the flight campaign names in Figure S3 are the number of .04 Hz in-cloud data points that match the latitude and altitude criteria.

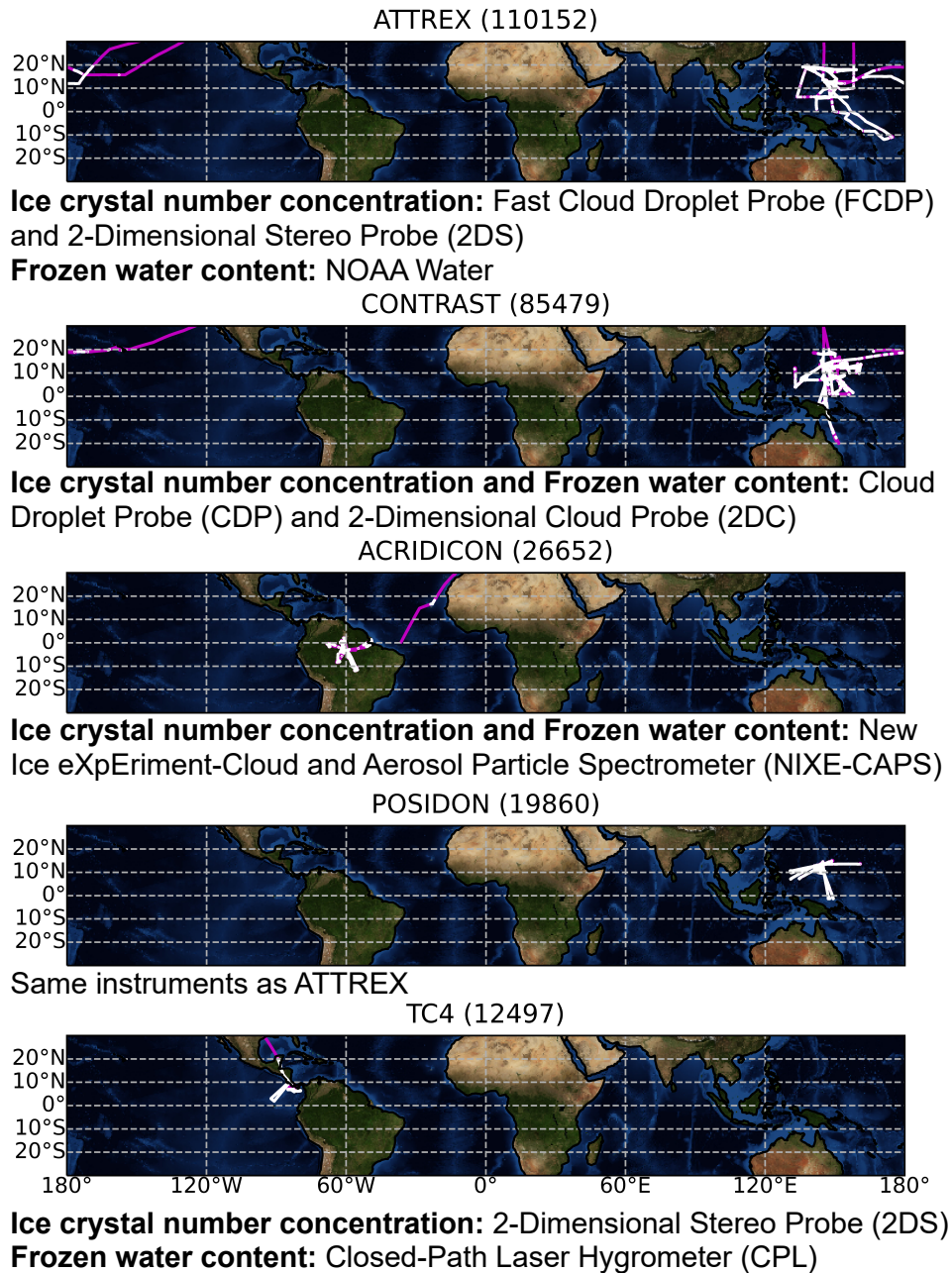


Figure S3. Campaign flight tracks in magenta with white overlay indicating in-cloud data above 10 km and within 20°N and 20°S. Map titles include the campaign name and the number of .04 Hz data points used in parentheses. Below each map, instruments used to measure or compute FWC and N_{ice} are listed.

Movie S1. For each hour of output from days 2-5 of the simulations, we show **left:** Snapshots of simulated frozen water path (FWP, including cloud ice, snow and graupel) for columns with cloud top height (CTH) > 10 km on the simulations' native grid and **right:** Coincident snapshots of longwave CRE bias compared to CERES on a coarsened $1^\circ \times 1^\circ$ grid. At high zenith angles, CERES sometimes mistakes land for cloud, causing a positive (blue) bias over the land. This is especially evident over Africa.